



**HAL**  
open science

# A general mathematical model for the in vitro assembly dynamics of intermediate filament proteins

Norbert Mücke, Tomasz Wocjan, Marine Jacquier, Harald Herrmann,  
Stéphanie Portet

► **To cite this version:**

Norbert Mücke, Tomasz Wocjan, Marine Jacquier, Harald Herrmann, Stéphanie Portet. A general mathematical model for the in vitro assembly dynamics of intermediate filament proteins. *Biophysical Journal*, 2022, 121 (6), pp.1094-1104. 10.1016/j.bpj.2022.02.001 . hal-03578492

**HAL Id: hal-03578492**

**<https://hal.science/hal-03578492>**

Submitted on 11 Apr 2022

**HAL** is a multi-disciplinary open access archive for the deposit and dissemination of scientific research documents, whether they are published or not. The documents may come from teaching and research institutions in France or abroad, or from public or private research centers.

L'archive ouverte pluridisciplinaire **HAL**, est destinée au dépôt et à la diffusion de documents scientifiques de niveau recherche, publiés ou non, émanant des établissements d'enseignement et de recherche français ou étrangers, des laboratoires publics ou privés.



Distributed under a Creative Commons Attribution - NonCommercial 4.0 International License

# A general mathematical model for the *in vitro* assembly dynamics of intermediate filament proteins

Norbert Mücke<sup>1,2</sup>, Tomasz Wocjan<sup>2</sup>, Marine Jacquier<sup>3</sup>, Harald Herrmann<sup>4</sup>, and Stéphanie Portet<sup>5,\*</sup>

<sup>1</sup>Chromatin Networks, German Cancer Research Center (DKFZ), Im Neuenheimer Feld 280, 69120 Heidelberg, Germany

<sup>2</sup>Biophysics of Macromolecules, German Cancer Research Center (DKFZ), Im Neuenheimer Feld 280, 69120 Heidelberg, Germany

<sup>3</sup>University of Rennes, CNRS, IGDR-UMR 6290, F-35000 Rennes, France

<sup>4</sup>Institute of Neuropathology, University Hospital Erlangen, Friedrich-Alexander University Erlangen-Nürnberg, 91054 Erlangen, Germany

<sup>5</sup>Department of Mathematics, University of Manitoba, 186 Dysart road, Winnipeg Manitoba R3T 2N2, Canada

\*Correspondence: [Stephanie.Portet@umanitoba.ca](mailto:Stephanie.Portet@umanitoba.ca)

**ABSTRACT** Intermediate filament (IF) proteins assemble into highly flexible filaments that organize into complex cytoplasmic networks: keratins in all types of epithelia, vimentin in endothelia and desmin in muscle. Since IF elongation proceeds via end-to-end annealing of unit-length filaments and successively of progressively growing filaments, it is important to know, how their remarkable flexibility, i.e., their persistence length  $l_p$ , influences the assembly kinetics. In fact, their  $l_p$  ranges between 0.3  $\mu\text{m}$  (keratin K8/K18) and 1.0  $\mu\text{m}$  (vimentin and desmin), and thus is orders of magnitude lower than that of microtubules and F-actin. Here, we present a unique mathematical model, which implements the semiflexible nature of the three IF types based on published semiflexible polymers theories and depends on a single free parameter  $k_0$ . Calibrating this model to filament mean length dynamics of the three proteins, we demonstrate that the persistence length is indeed essential to accurately describe their assembly kinetics. Furthermore, we reveal that the difference in flexibility alone does not explain the significantly faster assembly rate of keratin filaments compared to that of vimentin. Likewise, desmin assembles  $\sim$  six times faster than vimentin, even though both their filaments exhibit the same  $l_p$  value. These data strongly indicate that differences in their individual amino acid sequences significantly impact the assembly rates. Nevertheless, using a single  $k_0$  value for each of these three key representatives of the IF protein family, our advanced model does accurately describe the length distribution and mean length dynamics and provides effective filament assembly rates. It thus provides a tool for future investigations on the impact of post-translational modifications or amino acid changes of IF proteins on assembly kinetics. This is an important issue, as the discovery of mutations in IF genes causing severe human disease, particularly for desmin and keratins, is steadily increasing.

**SIGNIFICANCE** A single free parameter model for *in vitro* assembly kinetics of different types of intermediate filament (IF) proteins is proposed. IFs are highly flexible structures; the model implements filament semiflexible properties. Model calibration only necessitates filament mean length dynamics. We demonstrate that effective association rates required to describe assembly dynamics depend on filament contour and persistence lengths. Keratin, desmin and vimentin exhibit significantly different assembly kinetics, which cannot be explained solely by their respective persistence lengths. Instead, amino acid motifs outside of the two conserved IF homology domains mediating filament elongation must be considered as relevant determinants of assembly kinetics. A systematic tool is presented to investigate the impact of assembly conditions and amino acid modifications on IFs assembly dynamics.

## INTRODUCTION

Intermediate filaments (IF) are, in addition to microtubules and microfilaments, essential components of the metazoan cytoskeleton (1). The 70 genes coding for the IF multiprotein family are expressed in tissue-specific programs (2, 3). Hence, cells of mesenchymal origin express vimentin whereas smooth, cardiac and skeletal muscle express the sequence-related molecule desmin. Early in embryogenesis, both vimentin and desmin are coexpressed and form copolymers during the formation of muscle (4). In epithelia, the highly complex IF subfamily of keratins is expressed in tissue-specific patterns. In stark contrast

to the globular tubulins and actins, the constituents of microtubules and microfilaments, respectively, IF proteins are fibrous molecules that are characterized by the existence of an approximately 46 nm-long  $\alpha$ -helical domain in the center of the molecule (5). Under physiological conditions, two such  $\alpha$ -helices form a coiled coil. Despite of some amino acid sequence differences, vimentin and desmin are able to form not only homodimers but also heterodimers with one another. In stark contrast, keratins form obligate heterodimers from proteins of two sequence-related subgroups classified as “basic” and “acidic”, respectively.

In cells and tissues, IFs form networks that are insoluble during conventional extraction procedures. After forced expression in bacteria, IF proteins are deposited in insoluble inclusion bodies as well, and monomers are only obtained by solubilization with strong denaturants. The smallest subunits of IF proteins obtainable in non-denaturing conditions are tetramers, which are complexes assembled from two coiled coil dimers in an anti-parallel and half-staggered fashion. The *in vitro* IF assembly process is initiated by the rise of the ionic strength and is characterized by two distinct phases: first, tetramers laterally aggregate to form oligomers, in particular octamers, 16-mers and higher complexes. Lateral aggregation, which is finished within about a second of assembly, yields so-called unit-length-filaments (ULF), which are  $\sim 60$  nm long and 12-17 nm in diameter due to their heterogeneous composition. In the second, much slower phase, filament elongation takes place through the longitudinal annealing of ULFs and growing filaments with each other. The time-dependent length distributions of individual filaments can be measured by electron microscopy as well as by atomic force microscopy. As evident from the direct visualization of filaments, the short filaments generated early on can be treated as stiff rods, whereas the long filaments with a length well beyond the persistence length explicitly present as flexible polymers. The flexible nature of long filaments has also been demonstrated in solution by microfluidic methods employing fluorescently labelled IF proteins (6). Of note, the persistence length  $l_p$  of keratin filaments has been determined to be  $\sim 0.3 \mu\text{m}$ , whereas that of vimentin and desmin filaments is considerably larger with  $\sim 1.0 \mu\text{m}$  (7, 8). These values contrast strongly with those determined for F-actin,  $\sim 17\mu\text{m}$ , and microtubules,  $\sim 1400\mu\text{m}$  (9, 10).

We first obtained quantitative data of the *in vitro* vimentin filament elongation process by using a set of binding constants for the individual assembly steps in the formation of the various complexes (11). Based on these data, we generated models for the aggregation of linear macromolecules using the derivation of annealing rates for rigid rod-like elements (12, 13). Using light scattering and scanning transmission electron microscopy in combination with a modified Hill model, the kinetics of the vimentin assembly process was described in an ion strength dependent manner by Lopez *et al.* (14, 15). With our approach, we were able to fit *in vitro* vimentin length distributions over the first 20 minutes quite well, when filaments were shorter than the persistence length. However, this model did not accommodate length distributions at later time points, 20 minutes to 4 hours, as now filaments are on average longer than the respective persistence length (16). Thus, we concluded that the flexibility of IFs must play a role in their assembly process, in particular the productive encounter of the filaments ends. Using a Monte Carlo Simulation approach to investigate the kinetics of filament assembly, now with the filament flexibility as a key parameter, the *in vitro* vimentin IF length distributions at distinct mean lengths were well described by means of the computational model (17). In addition, this model was successfully applied to describe the assembly kinetics of desmin and keratin K8/K18, too. Thus, it was demonstrated that the *in vitro* filament elongation of these three different IF proteins, exhibiting quite different kinetics of assembly, can be described by the same mathematical principles on the basis of their shared principal molecular mechanism of assembly. Furthermore, these simulations demonstrated that the flexibility of IFs is important to accurately model the reaction rates for filament elongation.

As a next step in the analysis of IF assembly, we now generate a quantitative description of the annealing rates and therefore of the elongation reaction, as we now treat the model for the dynamics of filament assembly with a new expression for the association rate constants, inspired by previous concepts for semiflexible polymers (18, 19). Diffusion-controlled reaction rates incorporate filament shape fluctuations and hydrodynamics. The model is ultimately calibrated to experimental assembly kinetics data of keratin, desmin and vimentin and are thus verified by the experiments.

## MATERIALS AND METHODS

### Experimental data – Filament assembly conditions

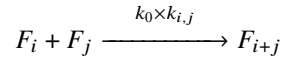
Experimental data used here consist of collections of filaments whose lengths are measured at different time points over the assembly process (13, 16, 17). Then, experimental length distributions and mean lengths are computed for the different time points. Filament length distributions and mean lengths at various time points of assembly used here to calibrate the model for keratin, desmin and vimentin have previously been published in (13, 16, 17).

Desmin and vimentin assembly is carried out in a phosphate buffer whereas keratin is assembled in Tris buffer. Aliquot amounts of keratin K8 and K18 were mixed in 8M urea and renatured into 2 mM Tris-HCl, pH 9.0. Assembly was initiated by addition of an equal volume of 18 mM Tris-HCl, pH 7.0 (*Tris-HCl assembly buffer*) yielding 10 mM Tris-HCl, pH 7.4, all calibrated to 37°C. Desmin and vimentin were renatured from 8 M urea by dialysis into 2 mM sodium phosphate, pH 7.5 (phosphate buffer). For both desmin and vimentin, the assembly was started at 37°C by addition of an equal volume of

phosphate buffer containing 200 mM potassium chloride to yield 2 mM NaPi, pH 7.5, 100 mM potassium chloride (*NaPi assembly buffer*). The protein concentration is 0.0025g/l for keratins and 0.1g/l for desmin and vimentin.

## Filament assembly model

To study the *in vitro* assembly kinetics of intermediate filaments, we modelled the dynamics of assembly of individual filaments on the basis of their length distributions and mean lengths. Similarly to the model in (13) and (16) we assume that only the polymer ends are reactive and that the association kinetics depend on the filaments length. With  $F_i$  being the time-dependent concentration of filaments composed of  $i$  ULFs, the association reaction between two filaments of length  $i$  and  $j$  associating to a total length  $i + j$  is as follows:



The effective association rate is given by  $k_0 \times k_{i,j}$ , where  $k_{i,j}$  is the diffusion-controlled association rate of two reactive sites approaching within the reaction distance (the maximum distance between the ends of two filaments allowing their association), while the prefactor  $k_0$  represents an intrinsic bimolecular rate constant. The diffusion-controlled association rates  $k_{i,j}$  are here approximated using the semiflexible polymer theory; hence, they depend on the interacting filaments contour lengths  $i$  and  $j$  as well on the filament persistence length  $l_p$  describing their flexibility. Derivation of  $k_{i,j}$  is given in the next section. It is assumed that the prefactor  $k_0$  affects the rate of assembly of filaments of any lengths in the same manner. Note that disassembly, dissociation or fragmentation/severing events, as seen in living cells due to kinase activities, are not described in the model, because they are not observed in the experimental *in vitro* set-up considered in this study (20).

The complete set of reactions between filaments of different lengths is then described by the following system of ordinary differential equations according to (21):

$$\frac{1}{k_0} \frac{dF_i}{dt} = \frac{1}{2} \sum_{j=1}^{i-1} (1 + \delta_{j,i-j}) k_{j,i-j} F_j F_{i-j} - \sum_{j=1}^{2N} (1 + \delta_{j,i}) k_{j,i} F_j F_i \quad (1)$$

where  $F_i$  is the time-dependent concentration of filaments of length  $i$  ULFs,  $\delta_{j,i}$  is the Kronecker function and the rate constants are symmetric  $k_{i,j} = k_{j,i}$ . The parameter  $N$  represents the maximal filament length in number of ULFs;  $2N$  is used for avoiding boundary effects in the numerical computations of system solutions. The prefactor  $k_0$  is the unique free parameter of the model, and it is estimated by fitting experimental data. At  $t = 0$  only ULFs are present in the experimental *in vitro* set-up considered in this study; therefore, the initial conditions are  $F_1(0) = c$ , with  $c > 0$ , and  $F_i(0) = 0$ ,  $\forall i > 1$ .

To compare to experimental data, the model length distributions are obtained from the proportions of filaments of length  $i$  at time  $t$ ,  $P_i(t)$ , and defined as

$$\forall i = 1, \dots, N, \quad P_i(t) = \frac{F_i(t)}{\sum_{i=1}^N F_i(t)}, \quad (2)$$

and the model mean length of filaments in number of ULFs at time  $t$ ,  $ML(t)$ , is given by

$$ML(t) = \sum_{i=1}^N i \left[ \frac{F_i(t)}{\sum_{i=1}^N F_i(t)} \right]. \quad (3)$$

## The diffusion-controlled reaction rate constant $k_{i,j}$

During filament growth, the intermediate filaments assemble from ULFs, which are the smallest filament units. They can be treated as stiff rods, to flexible polymers with length well beyond their persistence length  $l_p$ . Therefore, an appropriate model to accurately describe intermediate filaments must incorporate the flexibility of polymers and reproduce correctly the cross-over behaviour from stiff rods to flexible polymer coils.

An analytically tractable model to describe the dynamics of a semiflexible polymer is the semiflexible Gaussian chain model (22), where the polymer is represented as a continuous, differentiable space curve  $\mathbf{r}(s)$  of total length  $L$  with the parameter  $-L/2 \leq s \leq L/2$  defining the position on the polymer contour. It is based on the worm-like chain (WLC), where the bending energy is given by (23),  $U_{\text{WLC}}[\mathbf{r}(s)] = \frac{1}{2} k_B T l_p \int (\partial_s \mathbf{u}(s))^2 ds$ , with Boltzmann's constant  $k_B$  and the temperature  $T$ . Here  $\mathbf{u} = \partial_s \mathbf{r}(s)$  denotes the tangent vector at the polymer contour with the local constraint of inextensibility,  $|\mathbf{u}(s)| = 1$ , at each point  $s$  on the polymer contour. As shown by (24), using the mean-field theory, the relaxation of this local constraint to  $\langle \mathbf{u}(s)^2 \rangle = 1$  leads to an analytically tractable model with elastic energy  $U_{\text{MF}}[\mathbf{r}(s)] = \frac{\epsilon}{2} \int (\partial_s \mathbf{u}(s))^2 ds + \nu \int \mathbf{u}^2(s) ds + \nu_0 (\mathbf{u}^2(L/2) + \mathbf{u}^2(-L/2))$ ,

where  $\epsilon$ ,  $\nu$ , and  $\nu_0$  are constants. For the mean-field theory model it was shown that it yields the same equilibrium averages as mean-squared end-to-end distances, radius of gyration or tangent vector correlation function as the WLC (19).

The dynamics of a single point on the contour of a Gaussian semiflexible chain can be described by the Langevin equation  $\partial_t \mathbf{r}(s, t) = -\int \boldsymbol{\mu}_{avg}(s, s') \delta U_{MF} / \delta \mathbf{r}(s', t) ds' + \boldsymbol{\xi}(s, t)$ . Here  $\boldsymbol{\xi}(s, t)$  is the stochastic term, and  $\boldsymbol{\mu}_{avg}$  is the preaveraged mobility tensor, which takes into account long-range hydrodynamic interactions between points on the polymer. The preaveraged mobility tensor is calculated via a preaveraging approximation from the Rotne-Prager tensor (22, 25). The Langevin equation can be rewritten by expanding  $\mathbf{r}(s, t)$  and  $\boldsymbol{\xi}(s, t)$  in normal modes and amplitudes, which yields a set of partial differential equations for the normal mode amplitudes coupled by the hydrodynamic interaction matrix. Diagonalization allows to write the equations in terms of decoupled normal modes, which are effective on different time and length scales  $\tau_n$  and  $\Delta_n$ .

In the work of von Hansen *et al.* (18), the following Green's function based on the Gaussian semiflexible polymer model was derived and gives the probability that a point on the polymer contour starting at a position  $\mathbf{r}_0$  will be at the position  $\mathbf{r}$  after time  $t$

$$G(\mathbf{r}, \mathbf{r}_0; t) = (2\pi V_{pol}(t))^{-3/2} \exp\left(-\frac{(\mathbf{r} - \mathbf{r}_0)^2}{2V_{pol}(t)}\right) \quad (4)$$

$$V_{pol}(t) = 2D_{pol}t + \sum_{n=1}^{N_{pol}} \frac{\Delta_n}{3} (1 - \exp(-t/\tau_n)). \quad (5)$$

The first term of the variance  $V_{pol}(t)$  represents the center-of-mass diffusion of the polymer with the center-of-mass diffusion coefficient  $D_{pol}$  of the polymer coil; while the second term stems from the contributions of the internal polymer motion on different length scales  $\Delta_n$  and time scales  $\tau_n$ . As previously mentioned,  $\Delta_n$  and  $\tau_n$  are obtained from the hydrodynamic interaction matrix and the normal modes of the Langevin equation describing the dynamics of  $\mathbf{r}(s, t)$  (18). To compute  $\Delta_n$  and  $\tau_n$ , which depend on the contour and persistence lengths of the polymer, the approach followed in (18, 19) is used; further details are given in Supporting Material.

In the following we want to obtain the association kinetics between two semiflexible polymers. We follow hereby further the approach as outlined in Hansen *et al.* (18). They calculated kinetic rates in diffusion-limited reactions between a diffusing particle and a target site on a semiflexible polymer from the dynamic Green's function describing the time-dependent relative distance between the two reactive sites. The underlying assumption is that for the occurrence of the association of two polymers the reaction sites located at the polymer ends must be sufficiently close within a reaction distance  $r_{abs}$ .

According to (18) the radial Green's function for the case that two target sites starting with a separation  $r_0$  will be separated by a distance  $r$  after time  $t$  has the following form,

$$G_{rad}(r, r_0; t) = \frac{r}{r_0 \sqrt{2\pi \tilde{V}(t)}} \left[ \exp\left(-\frac{(r - r_0)^2}{2\tilde{V}(t)}\right) - \exp\left(-\frac{(r + r_0)^2}{2\tilde{V}(t)}\right) \right] \quad (6)$$

and it is obtained by integrating  $G(\mathbf{r}, \mathbf{r}_0; t)$  defined in Eq. 4 on the sphere of radius  $r$  for two polymers originally separated by a distance  $r_0$ . In the case that the target sites are totally decoupled, the variance  $\tilde{V}(t)$  then depends on the characteristics of both polymers and is given by

$$\begin{aligned} \tilde{V}(t) &= V_{pol,i}(t) + V_{pol,j}(t) \\ &= 2(D_{pol,i} + D_{pol,j})t + \sum_{n=1}^{N_i} \frac{\Delta_{n,i}}{3} (1 - \exp(-t/\tau_{n,i})) + \sum_{n=1}^{N_j} \frac{\Delta_{n,j}}{3} (1 - \exp(-t/\tau_{n,j})) \end{aligned} \quad (7)$$

with  $\Delta_{n,i}$ ,  $\tau_{n,i}$  and  $D_{pol,i}$  are the length scales, time scales and center-of-mass diffusion coefficients of the polymer of length  $L_i$  (respectively for  $L_j$ ). As for Eq. 5,  $D_{pol,i}$ ,  $\Delta_{n,i}$  and  $\tau_{n,i}$  depend on the properties of the filaments composed of  $i$  ULFs; its contour and persistence lengths,  $L_i$  and  $l_p$ .

The radial Green's function evaluated at the distance allowing a reaction  $r = r_{abs}$ ,  $G_{rad}(r_{abs}, r_0; t)$ , is related via the following equation

$$G_{rad}(r_{abs}, r_0; t) = \int_0^t f(t'; r_{abs}, r_0) G_{rad}(r_{abs}, r_{abs}; t - t') dt' \quad (8)$$

to the first passage time distribution  $f(t; r_{abs}, r_0)$ , which gives the probability of reaching  $r_{abs}$  in time  $t$  starting from the initial position  $r_0$  at time  $t = 0$  without passing through  $r_{abs}$ . On the other hand, the binding rate can be obtained from the first passage time distribution by averaging over all initial separations

$$k(t) = 4\pi \int_{r_{abs}}^{\infty} r_0^2 f(t; r_{abs}, r_0) dr_0. \quad (9)$$

The association rate  $k_{i,j}$  reached at long times is obtained via the final value theorem

$$k_{i,j} = \lim_{t \rightarrow \infty} k(t) = \lim_{s \rightarrow 0} s \tilde{k}(s) \quad (10)$$

where  $\tilde{k}(s)$  is obtained by applying the Laplace transform to Eq. 9, which yields  $\tilde{k}(s) = 4\pi \int_{r_{abs}}^{\infty} r_0^2 \tilde{f}(s; r_{abs}; r_0) dr_0$  with the frequency domain variable  $s$  from Eq. 9. The Laplace transform of the first-passage time distribution  $\tilde{f}(s; r_{abs}; r_0)$  is then obtained by applying the Laplace transform to Eq. 8 and re-arranging it that yields  $\tilde{f}(s; r_{abs}, r_0) = \tilde{G}_{rad}(r_{abs}, r_0; s) / \tilde{G}_{rad}(r_{abs}, r_{abs}; s)$ , where  $\tilde{G}_{rad}(r_{abs}, \cdot; s)$  is the Laplace transform of the radial Green's function  $G_{rad}(r_{abs}, \cdot; t)$  given in Eq. 6.

For numerical computations, we assumed that the reaction distance is of the order of the filament diameter; therefore, we set the reaction distance  $r_{abs} = 10$  nm. The Laplace transforms and integrations are numerically computed using the routines `gsl_integration_qagui` and `gsl_integration_qag` (26). To keep the computational effort reasonable, reaction rates  $k_{i,j}$  were calculated for filaments with a maximal number of  $\mathcal{N} < 2N$  ULFs, for multiple persistence lengths. For filaments with more than  $\mathcal{N}$  ULFs, we assume that kinetic rates remain practically length-independent. In this case the rate constants are approximated by  $k_{i,j} \approx k_{i,\mathcal{N}}$  for  $j \geq \mathcal{N}$  keeping in mind the symmetry  $k_{i,j} = k_{j,i}$ .

### Model calibration and prefactor $k_0$ estimation

In the derivation for diffusion-controlled reaction rates  $k_{i,j}$ , an elongation event (assembly of two filaments) occurs when the ends of the polymers exhibit a distance up to  $r_{abs}$ . The ends of polymers are described as spheres whose the entire surface is reactive allowing the assembly of kinked filaments. However, in electronic or atomic force microscopy images, kinked filaments are not observed (11). Hence, to preclude kinked filaments, only reactive caps of spheres have to be assumed yielding a slow down of  $k_{i,j}$ . Furthermore, other factors such as electrostatic interactions between polymer ends can affect the association kinetics. Hence, the effective rate of assembly for filaments of lengths  $i$  and  $j$  ULFs is  $k_0 \times k_{i,j}$ , where the prefactor  $k_0$  is the unique free parameter of the model Eq. 1 to estimate by fitting experimental data.

Calibration of model responses to experimental data can be carried out using either the length distributions with Eq. 2 or mean lengths with Eq. 3. When using length distributions, weighted errors must be considered to avoid over-expressing the contributions of early time points to the global error (13). Therefore, the prefactor  $k_0$  is estimated by using mean lengths, i.e., minimizing the distance between experimental and model mean lengths of filaments defined as follows

$$\Phi(k_0) = \sum_{j=1}^M (ML_{model}(t_j, p) - ML_{data}(t_j))^2, \quad (11)$$

where  $M$  is the number of time points, and  $ML_{model}(t_j, p)$  defined by Eq. 3 and  $ML_{data}(t_j)$  are the model and experimental mean lengths at time  $t_j$  respectively. The least-squares estimate  $\hat{k}_0$  is defined such that

$$\Phi(\hat{k}_0) = \min_{k_0} \Phi(k_0). \quad (12)$$

The minimization is numerically solved by using `fmin` function in Matlab or a global optimisation method, the genetic algorithm coded in the R package `GA` (27). Furthermore, the likelihood ratio statistic is introduced to estimate confidence intervals for  $k_0$  (28). The  $100(1 - \alpha)\%$  confidence intervals for  $k_0$  are composed of  $k_0$  values whose the log-likelihood function  $\ln L(k_0)$  value satisfies  $\ln L(k_0) > \ln L(\hat{k}_0) - \chi_{1,\alpha}^2/2$ , where  $\chi_{1,\alpha}^2$  is the value of the  $(1 - \alpha)\%$  centile of the chi-squared distribution on one degree of freedom. Assuming independent and normally distributed additive measurement errors with the same variance, the negative of the log-likelihood of a value of the parameter  $k_0$  given the data considered,  $-2 \ln L(k_0)$ , is approximated by  $M \ln(\Phi(k_0)/M)$  (29, 30).

## RESULTS AND DISCUSSION

### Persistence length dependence of the reaction rates $k_{i,j}$

For computing diffusion-controlled reaction rates  $k_{i,j}$ , we describe polymers using the IF characteristics. The filament diameter is set to  $d = 10$  nm and length is expressed in number  $i$  of ULFs. Note that due to ULF interdigitation, the first ULF contributes 60 nm to the filament length, while further ULF increases the length by approximately 43 nm. An IF composed of  $i$  ULFs has the length  $L_i$  (in nm),  $L_i = (i - 1)m + n$  with  $m = 43$  nm and  $n = 60$  nm (13). As previously mentioned, it is assumed that the reaction distance  $r_{abs}$  is of the order of the filament diameter; therefore, we used  $r_{abs} = 10$  nm in the numerical calculations. Using structural features of IFs, we computed  $k_{i,j}$  for three persistence lengths  $l_p = 333, 500$  and  $1000$  nm. For  $l_p = 333$  nm,

$k_{i,j}$  are explicitly computed for  $i$  and  $j$  up to  $\mathcal{N} = 130$  ULFs, for  $l_p = 500$  nm,  $\mathcal{N} = 100$  ULFs and for  $l_p = 1000$  nm,  $\mathcal{N} = 180$  ULFs. Figure 1 shows the diffusion-controlled reaction rates  $k_{i,j}$  for the association of two polymers of length  $i$  and  $j$  ULFs with  $i, j \leq 100$  ULFs. The  $k_{i,j}$  values are provided in Supporting Material.

For a given persistence length  $l_p$ ,  $k_{i,j}$  values decrease as the interacting objects length increases but span a small range. For instance, with  $i$  and  $j$  between 1 to 100 ULFs,  $k_{i,j}$  values for long filaments are at most 30 percent smaller than for short filaments (Figure 1A). The smaller the persistence length, the larger  $k_{i,j}$ . For long filaments, values for  $k_{i,j}$  obtained with  $l_p = 1000$  nm are about 10% smaller than with  $l_p = 333$  nm (Figure 1B).

Figure 1: (A) Diffusion-controlled reaction rates  $k_{i,j}$  for different persistence lengths  $l_p = 333, 500$  and  $1000$  nm. (B)  $k_{1,j}$ ,  $k_{5,j}$  and  $k_{20,j}$ .

## Determinants of filament length distributions and of mean length dynamics

The dynamics of filament length distributions and mean lengths are obtained from numerical solutions of Eq. 1 via Eq. 2 and Eq. 3 respectively. The filament mean length (ML) is used as a polymerization/assembly degree to characterize the effect of the prefactor  $k_0$  and persistence length  $l_p$  on the filament assembly kinetics before fitting model responses to experimental data. Here, the same protein concentration is used for all comparisons and it is set to  $c = 0.1$  g/l.

The prefactor  $k_0$  only tunes the assembly dynamics by speeding up or slowing down the process. With a persistence length  $l_p$ , the following scaling is observed,  $ML_{l_p}(t, k_0) = ML_{l_p}(t/k_0, 1)$  (Figure 2).

Figure 2: Effect of  $k_0$  on the assembly dynamics: illustration of the scaling  $ML_{l_p}(t, k_0) = ML_{l_p}(t/k_0, 1)$ . (A) For two persistence length values  $l_p = 333$  and  $1000$  nm, time evolution of mean lengths  $ML_{l_p}(t, k_0)$  obtained with  $k_0 = 0.001$  (time axis at the top) and  $k_0 = 1$  (time axis at the bottom). (B) With  $l_p = 333$  and  $1000$  nm, times to reach a mean length of 5 ULFs with different values for  $k_0$ .

Fixing the prefactor  $k_0$  value, effects of persistence length  $l_p$  on the mean length and distribution dynamics are then shown in Figure 3. As expected from our previous observations on  $k_{i,j}$  values, the longer the persistence length, the slower to reach a given mean length (Figure 3A and B). At the early stages of the assembly, the slowing-down of the dynamics observed with longer persistence lengths is not a linear process over time (Figure 3B). With a given mean length, the same length distributions are obtained for all the three persistence lengths (Figure 3C). Only the time to reach a given mean length varies but the shape of length distributions is not affected by the persistence length  $l_p$ .

Figure 3: Effect of persistence length  $l_p$  on mean length and length distribution dynamics with  $k_0 = 1$ . (A) Mean lengths obtained with  $l_p = 333, 500$  and  $1000$  nm over time. (B) Mean lengths are compared over time to those obtained with  $l_p = 333$  via  $ML_*(t)/ML_{333}(t)$ . At a given time, the mean length for  $l_p = 1000$  (resp.  $l_p = 500$ ) can be up to 6% (resp. 2%) smaller than those obtained with  $l_p = 333$ . (C) Distributions of lengths with a mean length of 3, 5 and 10 ULFs. Distributions with a given mean length obtained for the three different persistence lengths are the same and cannot be distinguished.

## Comparing keratin, desmin and vimentin assembly kinetics

The model Eq. 1 is then calibrated to *in vitro* assembly of keratin, desmin and vimentin filaments using Eq. 11 and the prefactor  $k_0$ , the unique model parameter, is estimated. *In vitro* experimental data used for the calibration are selected to ensure that the kinetics are comparable as one goal of the work is to provide with a systematic tool to measure/evaluate the assembly kinetics of different IF proteins. Hence, for the three proteins, four time points are selected for which experimental length distributions have a mean length in similar ranges. Recall that desmin and vimentin are assembled in the same buffer condition (NaPi buffer) with the same concentration whereas keratins are assembled in Tris-HCl buffer without monovalent ions and at a much lower protein concentration (31). Thereby, overshoot reactions resulting in lateral filament associations as shown in (32) are prevented. Details on proteins concentrations  $c$ , time points  $t$  and mean lengths  $ML$  used for keratin, desmin and vimentin are provided in Table 1. The experimental length distributions and mean lengths are shown in gray in Figure 4. A persistence length of  $l_p = 333$  nm is used to compute  $k_{i,j}$  for keratin filaments and  $l_p = 1000$  nm for desmin and vimentin filaments.

(a) Keratin			(b) Desmin			(c) Vimentin		
$c$	$t$	$ML$	$c$	$t$	$ML$	$c$	$t$	$ML$
0.0025	10	2.1	0.1	10	2.2	0.1	60	2.12
0.0025	60	3.7	0.1	30	3.8	0.1	300	5.27
0.0025	120	5.0	0.1	60	9.6	0.1	1200	9.23
0.0025	300	8.3	0.1	300	15.3	0.1	1800	19.2

Table 1: Details on data used for model calibration. Length distributions for (a) keratin, (b) desmin and (c) vimentin filaments are considered at four time points  $t$  with comparable mean lengths  $ML$ . Units for initial concentrations  $c$  are in  $g/l$ ,  $t$  are in seconds, and  $ML$  are in number of ULF.

Figure 4: Model calibration results to experimental filaments mean lengths. (A) Profiles for the three proteins of model prediction errors,  $\Phi(k_0)$  defined in Eq. 11, as a function of  $k_0$ . (B) Approximated likelihoods of the parameter  $k_0$ ,  $L(k_0)$ , for the three proteins used to compute the likelihood ratio confidence intervals. Shaded regions delimit the 90% confidence intervals (IC) of  $k_0$  for the three proteins. ICs are provided in (C) as well  $\hat{k}_0$  minimizing the errors (or maximizing the likelihood of  $k_0$  for the considered data). (D-F) Assembly dynamics of the three proteins (D) Keratin with  $c = 0.0025g/l$  in Tris-HCl buffer, (E) Desmin with  $c = 0.1g/l$  in NaPi buffer and (F) Vimentin with  $c = 0.1g/l$  in NaPi buffer. Experimental data are presented in gray: the first four panels show the filament length distributions at four time points and in addition the last panels show the mean lengths of filaments over time. Model length distributions and mean lengths are given in colors: plain curves are the best fits obtained with  $\hat{k}_0$  and shaded regions are delimited by the model responses obtained with  $k_0$  values within 90% confidence intervals.

For each protein, the model calibrated on the experimental mean lengths represents the complete dynamics both in terms of filament length distributions and mean lengths quite well: a single value of  $k_0$  is sufficient to represent the assembly kinetics over the four time points (Figure 4D-F). It is obvious from the locations of global extrema of prediction error or the corresponding approximated likelihood profiles that the suitable values for the prefactor to describe the assembly kinetics differ for the three proteins (Figure 4A-B). The 90% likelihood ratio confidence intervals for  $k_0$  are very narrow for the three proteins; confidence intervals are of the order of  $10^{-3}$  for keratin,  $10^{-4}$  for desmin and  $10^{-5}$  for vimentin (Figure 4C). Hence, the estimated optimal effective length-dependent rates  $\hat{k}_0 \times k_{i,j}$  are of order  $10^7 M^{-1}.s^{-1}$  for keratin,  $10^6 M^{-1}.s^{-1}$  for desmin and  $10^5 M^{-1}.s^{-1}$  for vimentin.

Distributions of optimal length-dependent effective association rates  $\hat{k}_0 \times k_{i,j}$  for the three proteins under the filament assembly conditions considered in this work are shown in Figure 5. The effective association rate of two ULFs,  $\max(\hat{k}_0 \times k_{i,j}) = \hat{k}_0 \times k_{1,1}$ , is estimated to  $16.3 \times 10^6 M^{-1}.s^{-1}$  for keratin,  $1.97 \times 10^6 M^{-1}.s^{-1}$  for desmin and  $0.35 \times 10^6 M^{-1}.s^{-1}$  for vimentin. The effective association rates for filaments shorter than 100 ULFs,  $[\min(\hat{k}_0 \times k_{i,j}), \max(\hat{k}_0 \times k_{i,j})]$  with  $i, j < 100$ , range in  $[11.2 \times 10^6, 16.3 \times 10^6] M^{-1}.s^{-1}$  for keratin,  $[1.29 \times 10^6, 1.97 \times 10^6] M^{-1}.s^{-1}$  for desmin and  $[0.23 \times 10^6, 0.35 \times 10^6] M^{-1}.s^{-1}$  for vimentin. The desmin assembly rate is about six time faster than that of vimentin under identical assembly conditions (NaPi assembly buffer). The keratin assembly kinetics, carried out with a 40 times lower concentration than for desmin and vimentin and in Tris-HCl buffer, is significantly enhanced compared to the two other proteins. Note that the diffusion-controlled reaction rates  $k_{i,j}$  are in the range of  $[4.44 \times 10^9, 6.27 \times 10^9]$  for  $l_p = 333nm$  and  $[4.18 \times 10^9, 6.14 \times 10^9]$  for  $l_p = 1000nm$  (Figure 5A); the effect of the persistence lengths on  $k_{i,j}$  and on the effective association rates is negligible.

Figure 5: (A) Distributions of length-dependent diffusion-controlled reaction rates  $k_{i,j}$  for filaments of lengths  $i$  and  $j < 100$  with  $l_p = 333$  and  $l_p = 1000$  nm as shown in Figure 1 and used for dynamics in Figure 4. (B) Distributions of length-dependent effective association rates  $\hat{k}_0 \times k_{i,j}$  yielding the best fits of experimental filament mean lengths in Figure 4D-F for keratin with  $c = 0.0025g/l$  in Tris-HCl buffer, desmin with  $c = 0.1g/l$  in NaPi buffer and vimentin with  $c = 0.1g/l$  in NaPi buffer. The tails of distributions or maximal values correspond to association rates of two ULFs;  $k_{1,1}$  in (A) and  $\hat{k}_0 \times k_{1,1}$  in (B).

Finally, more time points can be considered for calibrating the model. For instance, Figure 6 shows assembly dynamics of vimentin filaments over nine time points from 10 seconds to 4 hours; five time points are added to the dynamics previously considered in Figure 4F. The experimental assembly kinetics from 10 seconds to 4 hours is consistently described by the model; both length distributions and mean lengths are well represented at the nine time points (Figure 6D). The proposed model is

Figure 6: Assembly of vimentin: (Early - light blue) calibration is carried out with the assembly data from 1 to 30 minutes shown in Figure 4F, (Total - dark blue) calibration is carried out on assembly data from 10 seconds to 4 hours. The five additional time points considered are : 10 seconds with a ML of 1.12 ULFs, 30 seconds with a ML 1.64 ULFs, 10 minutes with a ML of 6.92 ULFs, 2 hours with a ML of 35 ULFs and 4 hours with a ML of 49 ULFs. (A) Profiles of model prediction errors  $\Phi(k_0)/M$  as a function of  $k_0$ , where  $\Phi(k_0)$  is defined in Eq. 11 and  $M$  is the number of time points composing the assembly dynamics. (B) Approximated likelihood profiles of the parameter  $k_0$  used to compute the likelihood ratio confidence intervals. Shaded regions delimit the 90% confidence intervals (IC) of  $k_0$ . ICs are provided in (C) as well  $\hat{k}_0$  minimizing the errors (or maximizing the likelihood of  $k_0$  for the considered data). (D) Experimental data are presented in gray and model predictions in colors: first nine panels show filament length distributions at nine time points, the last panels show the mean lengths of filaments over time. Plain curves are the best fits obtained with  $\hat{k}_0$  and shaded regions are delimited by the model responses obtained with  $k_0$  values from 90% confidence intervals provided in C.

found to capture correctly the length distribution shapes at any time considered, which was not the case of the previous models (16). Furthermore, fitting additional time points results in values for  $\hat{k}_0$  of the same order of  $10^{-5}$  as previously found for vimentin (Figure 4C). However, the model calibrated on mean lengths measured up to 30 minutes as shown in Figure 4F is found to have the poorest performance for representing the two and four hours length distributions shape and mean lengths; the model when calibrated on the early dynamics (up to 30 minutes) predicts faster assembly rates than the experimental observations at two and four hours. The  $\hat{k}_0^{Total}$  optimal value (and so effective rates) estimated on the data from 10 seconds to 4 hours is found to be smaller than  $\hat{k}_0^{Early}$  estimated on data up to 30 minutes:  $\hat{k}_0^{Early}/2 \approx \hat{k}_0^{Total}$  and their confidence intervals do not overlap (Figure 6). The slowdown of experimental assembly velocity after two hours might be explained by technical reasons. The assembly kinetics at two and four hours is observed with TIRF microscopy (33); the number of filaments actively engaged in assembly may decrease over time due to adsorption of increasingly longer filaments to the walls of the reaction vessels, thus leading to reduced values of assembly. Moreover, the model neglects excluded volume effects; these effects might increase the longer filaments become. A loss of activity of protein ends could furthermore be due to a change over time of filament properties due to rearrangements within filaments.

## CONCLUSION

The theory for semiflexible polymers used here to approximate the diffusion-controlled reaction rates  $k_{i,j}$  was previously developed in two independent studies (18, 19). It was demonstrated to be very successful at reproducing recent fluorescence correlation spectroscopy data, where the end-monomer motion of fluorophore-labelled dsDNA polymer was measured. There, the experimentally obtained mean-square displacement of the end-monomer matched the analytical result, which was further verified with Brownian dynamics simulations. This is interesting to note as dsDNA has a persistence length close to that of intermediate filaments, i.e., 50nm.

Combining these contour and persistence lengths-dependent association rates  $k_{i,j}$  with an aggregation model for the filament elongation dynamics controlled by a single free parameter  $k_0$ , we are able to describe the *in vitro* assembly kinetics of three intermediate filament proteins exhibiting significantly different amino acid sequences and persistence lengths, i.e., 0.3  $\mu\text{m}$  for keratin K8/K18 and 1.0  $\mu\text{m}$  for desmin and vimentin. In a previous work, the same aggregation model was used in combination with four other expressions for association rates with no proper description of filament flexibility; none of the four resulting models predicted accurate shapes of length distributions for the full dynamics (16). Here, the semiflexible chain model allows the use of a unique model depending on a single free parameter to accommodate the *in vitro* filament assembly dynamics of keratin, desmin and vimentin at different protein concentrations and assembly buffers. Moreover, for a given mean length, shapes of length distributions obtained with distinct persistence lengths do not differ indicating that the mode of filament elongation from common basic units (ULFs) as described in the model is the same for the three proteins. Furthermore, the proposed model can be calibrated to either experimental length distributions or mean lengths. Here, the model calibration is carried out using filaments mean lengths, nevertheless correct shapes for length distributions are recovered over time. Hence, the model with a single value of  $\hat{k}_0$  allows the estimation of the length distributions at the different times of the assembly dynamics when only the temporal evolution of the filament mean lengths is known. Estimated effective assembly rates  $\hat{k}_0 \times k_{i,j}$ , accounting for filament lengths and flexible properties via  $k_{i,j}$ , are adjusted to other protein specificity and filament assembly conditions via  $\hat{k}_0$ . In conclusion, we propose here a computational approach to fully characterize the *in vitro* assembly kinetics of intermediate filaments under various ionic assembly conditions and protein concentrations, which permit the elongation of individual filaments but prevent filament bundle formation, just from their mean length dynamics.

Finally, we found that *in vitro* assembly kinetics of vimentin is six times slower than that of desmin under the same assembly

conditions. With the data considered, keratin with a smaller protein concentration and in a low ionic strength buffer does elongate much faster than desmin and vimentin. The differences between keratin and desmin or vimentin kinetics cannot be explained by their difference in flexibility as the effect of persistence lengths on diffusion-controlled reaction rates in the range of lengths considered can only explain a change in the assembly dynamics lower than 10% (Figure 3B). Also, desmin and vimentin have the same persistence length and consequently the same values for diffusion-controlled reaction rates  $k_{i,j}$ , but the desmin effective association rate values are about six times larger than those of vimentin. Hence, accounting for filament flexibility is necessary to represent intermediate filaments assembly kinetics but it is not sufficient to explain the differences in kinetics of keratin and desmin or vimentin. Instead, it must be the differences originating in the primary amino acid sequences. Even though vimentin and desmin are 70% identical in the sequence of the central  $\alpha$ -helical rod domain, they show significant differences in the amino- and carboxy-terminal segments known to be important for the assembly reaction (34). The overall sequence identities are very much lower when keratin K8/K18 are compared with vimentin and desmin. Actually, it is practically only the two  $\sim 20$  amino acid-long terminal segments of the  $\alpha$ -helical rod domain, the so-called IF protein consensus motifs, which is evolutionarily highly conserved from invertebrate cytoplasmic IF proteins to human hair keratins (35, 36). These segments mediate the principal elongation reaction of IF when the amino-terminal ends of the  $\alpha$ -helical rod of one dimer within an ULF anneal to the carboxy-terminal ends of the  $\alpha$ -helical rod of a second dimer from an ULF to be longitudinally annealed (5). Hence, it is very likely that the strong amino acid sequence differences between vimentin and desmin as well as keratins outside of these hallmark segments, which mediate the direct physical overlap contacts for elongation, cause the protein-type specific kinetics. In particular, the ionic charges within the  $\alpha$ -helical rod domain of vimentin, desmin and keratins differ significantly, possibly explaining the observed differences in the impact of the buffer composition on assembly (15, 37).

In summary, our advanced model allows to compare the assembly kinetics of different intermediate filament proteins and provides a rigorous systematic tool to evaluate, for instance, the impact of assembly buffer conditions or amino acid modifications on the *in vitro* assembly process.

## AUTHOR CONTRIBUTIONS

NM, HH and SP designed the research. TW, MJ and SP carried out all simulations, analyzed the data. NM, HH and SP wrote the article. The theoretical part of this work has been developed by TW under the direction of Jörg Langowski who was the Head of the Division of Biophysics of Macromolecules at the DKFZ (German Cancer Research Center) in Heidelberg.

## DECLARATION OF INTERESTS

The authors declare no competing interests.

## ACKNOWLEDGMENTS

SP is supported in part by a Discovery Grant of the Natural Sciences and Engineering Research Council of Canada (RGPIN-2018-04967) and a Burroughs Wellcome Fund 2020 Collaborative Research Travel Grant. HH was supported by grants from the German Research Foundation (HE 1853/11).

## REFERENCES

1. Etienne-Manneville, S., 2018. Cytoplasmic intermediate filaments in cell biology. *Annu. Rev. Cell Dev. Biol.* 34:1–28.
2. Fuchs, E., and K. Weber, 1994. Intermediate filaments: Structure, Dynamics, Function and Disease. *Annu. Rev. Biochem.* 63:345–382.
3. Herrmann, H., M. Hesse, M. Reichenzeller, U. Aebi, and T. Magin, 2003. Functional complexity of intermediate filament cytoskeletons: from structure to assembly to gene ablation. *Int. Rev. Cytol.* 223:83–175.
4. Lazarides, E., 1982. Intermediate Filaments: A Chemically Heterogeneous, Developmentally Regulated Class of Proteins. *Annu. Rev. Biochem.* 51:219–250.
5. Herrmann, H., and U. Aebi, 2016. Intermediate Filaments: Structure and Assembly. *Cold Spring Harb. Perspect. Biol.* 8:a018242.
6. Köster, S., D. A. Weitz, R. D. Goldman, U. Aebi, and H. Herrmann, 2015. Intermediate filament mechanics in vitro and in the cell: from coiled coils to filaments, fibers and networks. *Curr. Opin. Cell Biol.* 32:82–91.

7. Mücke, N., L. Kreplak, R. Kirmse, T. Wedig, H. Herrmann, U. Aebi, and J. Langowski, 2004. Assessing the flexibility of intermediate filaments by atomic force microscopy. *J. Mol. Biol.* 335:1241–1250.
8. Mücke, N., K. Klenin, R. Kirmse, M. Bussiek, H. Herrmann, M. Hafner, and J. Langowski, 2009. Filamentous Biopolymers on surfaces: Atomic Force Microscopy images compared with Brownian dynamics simulation of filament deposition. *PLoS One* 4:7756–7763.
9. Isambert, H., P. Venier, A. Maggs, A. Fattoum, R. Kassab, D. Pantaloni, and M. Carlier, 1995. Flexibility of actin filaments derived from thermal fluctuations. Effect of bound nucleotide, phalloidin, and muscle regulatory proteins. *J. Biol. Chem.* 270:11437–44.
10. van Mameren, J., K. Vermeulen, F. Gittes, and C. Schmidt, 2009. Leveraging single protein polymers to measure flexural rigidity. *J. Phys. Chem. B* 113:3837–44.
11. Kirmse, R., S. Portet, R. Mücke, U. Aebi, H. Herrmann, and J. Langowski, 2007. A quantitative kinetic model for the in vitro assembly of intermediate filaments from tetrameric vimentin. *J. Biol. Chem.* 282:18563–18572.
12. Hill, T., 1983. Length dependence of rate constants for end-to-end association and dissociation of equilibrium linear aggregates. *Biophys. J.* 44:285–288.
13. Portet, S., N. Mücke, R. Kirmse, J. Langowski, M. Beil, , and H. Herrmann, 2009. Vimentin Intermediate Filament Formation: In Vitro Measurement and Mathematical Modeling of the Filament Length Distribution during Assembly. *Langmuir* 25:8817–8823.
14. Lopez, C., O. Saldanha, K. Huber, and S. Köster, 2016. Lateral association and elongation of vimentin intermediate filament proteins: A time-resolved light-scattering study. *Proc. Natl. Acad. Sci.* 113:11152–11157.
15. Lopez, C., O. Saldanha, A. Aufderhorst-Roberts, C. Martinez-Torres, M. Kuijs, G. H. Koenderink, S. Köster, and K. Huber, 2018. Effect of ionic strength on the structure and elongational kinetics of vimentin filaments. *Soft Matter* 14:8445–8454.
16. Portet, S., 2013. Dynamics of in vitro intermediate filament length distributions. *J. Theor. Biol.* 332:20–29.
17. Mücke, N., S. Winheim, H. Merlitz, J. Buchholz, J. Langowski, and H. Herrmann, 2016. In Vitro Assembly Kinetics of Cytoplasmic Intermediate Filaments: A Correlative Monte Carlo Simulation Study. *PLoS One* 11:e0157451.
18. von Hansen, Y., R. Netz, and M. Hinczewski, 2010. DNA-protein binding rates: Bending fluctuation and hydrodynamic coupling effects. *J. Chem. Phys.* 132:135103.
19. Hinczewski, M., X. Schlagberger, M. Rubinstein, O. Krichevsky, and R. Netz, 2009. End-Monomer Dynamics in Semiflexible Polymers. *Macromolecules* 42:860–875.
20. Nöding, B., H. Herrmann, and S. Köster, 2014. Direct observation of subunit exchange along mature vimentin intermediate filaments. *Biophys. J.* 107:2923–2931.
21. Khatouri, J., M. Mostafavi, J. Ridard, J. Amblard, and J. Belloni, 1995. Kinetics of cluster growth by aggregation. *Z. Phys. D* 34:47–56.
22. Harnau, L., R. Winkler, and P. Reineker, 1996. Dynamic structure factor of semiflexible macromolecules in dilute solution. *J. Chem. Phys.* 104:6355–6368.
23. Kratky, O., and G. Porod, 1949. Röntgenuntersuchung gelöster Fadenmoleküle. *Recl. Trav. Chim. Pays-Bas* 68:1106.
24. Winkler, R., P. Reineker, and L. Harnau, 1994. Models of equilibrium properties of stiff molecular chains. *J. Chem. Phys.* 101:8119–8129.
25. Rotne, J., and S. Prager, 1969. Variational Treatment of Hydrodynamic Interaction in Polymers. *J. Chem. Phys.* 50:4831.
26. Galassi, M., J. Davies, J. Theiler, B. Gough, G. Jungman, M. Booth, and F. Rossi. GNU Scientific Library Reference Manual (3rd edition).
27. Scrucca, L., 2013. GA: Genetics Algorithms.

28. Leemis, L., 2020. *Mathematical Statistics*. Lightning Source.
29. Baker, C., G. Bocharov, C. Paul, and F. Rihan, 2005. Computational modelling with functional differential equations: Identification, selection, and sensitivity. *Appl. Numer. Math.* 53:107–129.
30. Portet, S., 2020. A primer on model selection using the Akaike Information Criterion. *Infect. Dis. Model.* 5:111–128.
31. Lichtenstern, T., U. Mücke, N. Aebi, M. Mauermann, and H. Herrmann, 2012. Complex formation and kinetics of filament assembly exhibited by the simple epithelial keratins K8 and K18. *J. Struct. Biol.* 177:54–62.
32. Kayser, J., H. Grabmayr, M. Harasim, H. Herrmann, and A. Bausch, 2012. Assembly kinetics determine the structure of keratin networks. *Soft Matter* 8:8873–8879.
33. Winheim, S., A. Hieb, M. Silbermann, E.-M. Surmann, T. Wedig, H. Herrmann, J. Langowski, and N. Mücke, 2011. Deconstructing the late phase of vimentin assembly by total internal reflection fluorescence microscopy (TIRFM). *PLoS One* 6:e19202.
34. Schaffeld, M., H. Herrmann, J. Schultess, and J. Markl, 2001. Vimentin and desmin of a cartilaginous fish, the shark *Scyliorhinus stellaris*: Sequence, expression patterns and in vitro assembly. *Eur. J. Cell Biol.* 80:692–702.
35. Herrmann, H., S. Strelkov, B. Feja, K. Rogers, M. Brettel, A. Lustig, M. Häner, D. Parry, P. Steinert, P. Burkhard, and U. Aebi, 2000. The intermediate filament protein consensus motif of helix 2B: its atomic structure and contribution to assembly. *J. Mol. Biol.* 298:817–32.
36. Herrmann, H., and U. Aebi, 2004. Intermediate filaments: Molecular structure, assembly mechanism, and integration into functionally distinct intracellular scaffolds. *Annu. Rev. Biochem.* 73:749–789.
37. Denz, M., M. Marschall, H. Herrmann, and S. Köster, 2021. Ion type and valency differentially drive vimentin tetramers into intermediate filaments or higher order assemblies. *Soft Matter* 17:870–878.

## SUPPLEMENTARY MATERIAL

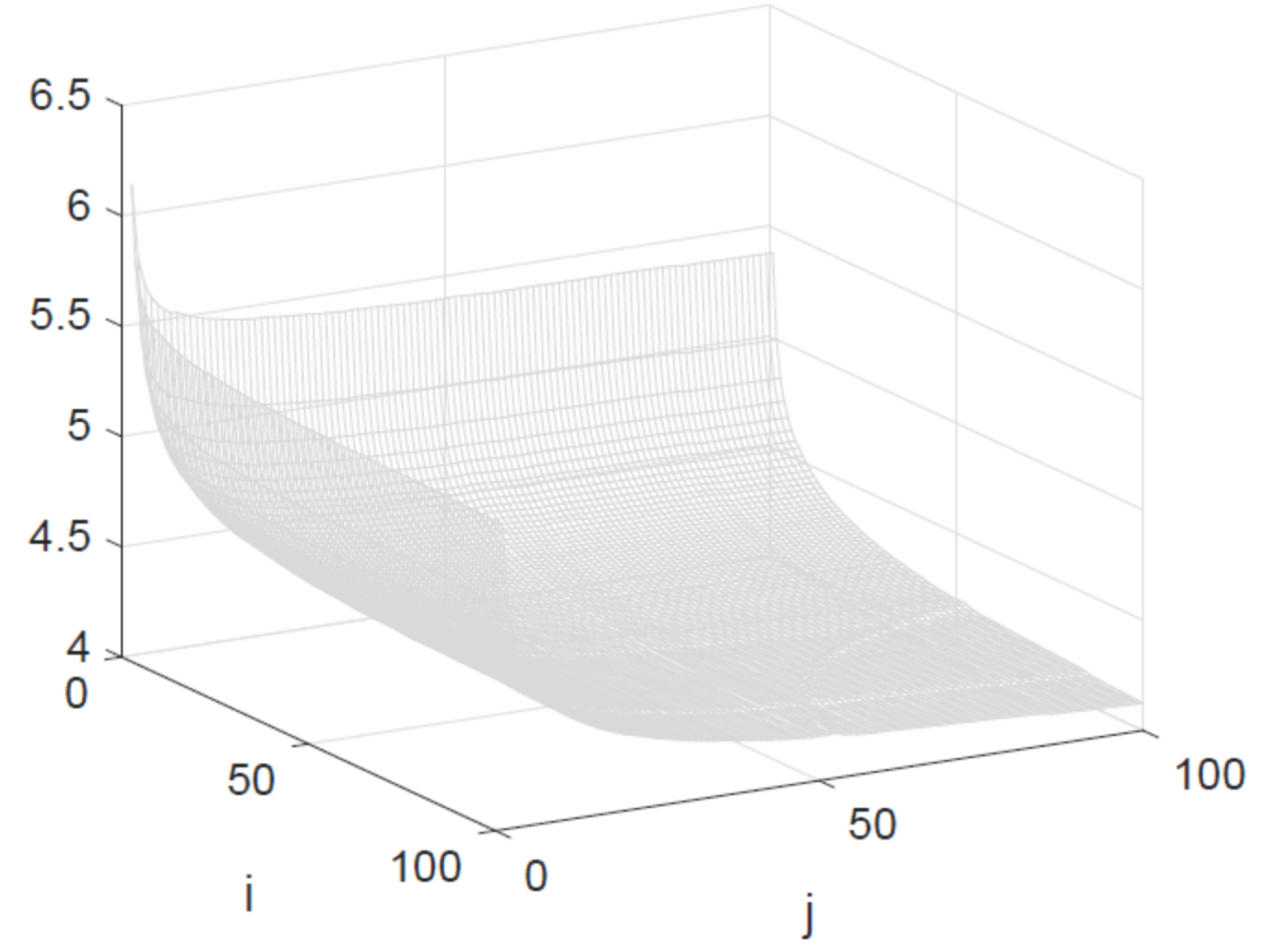
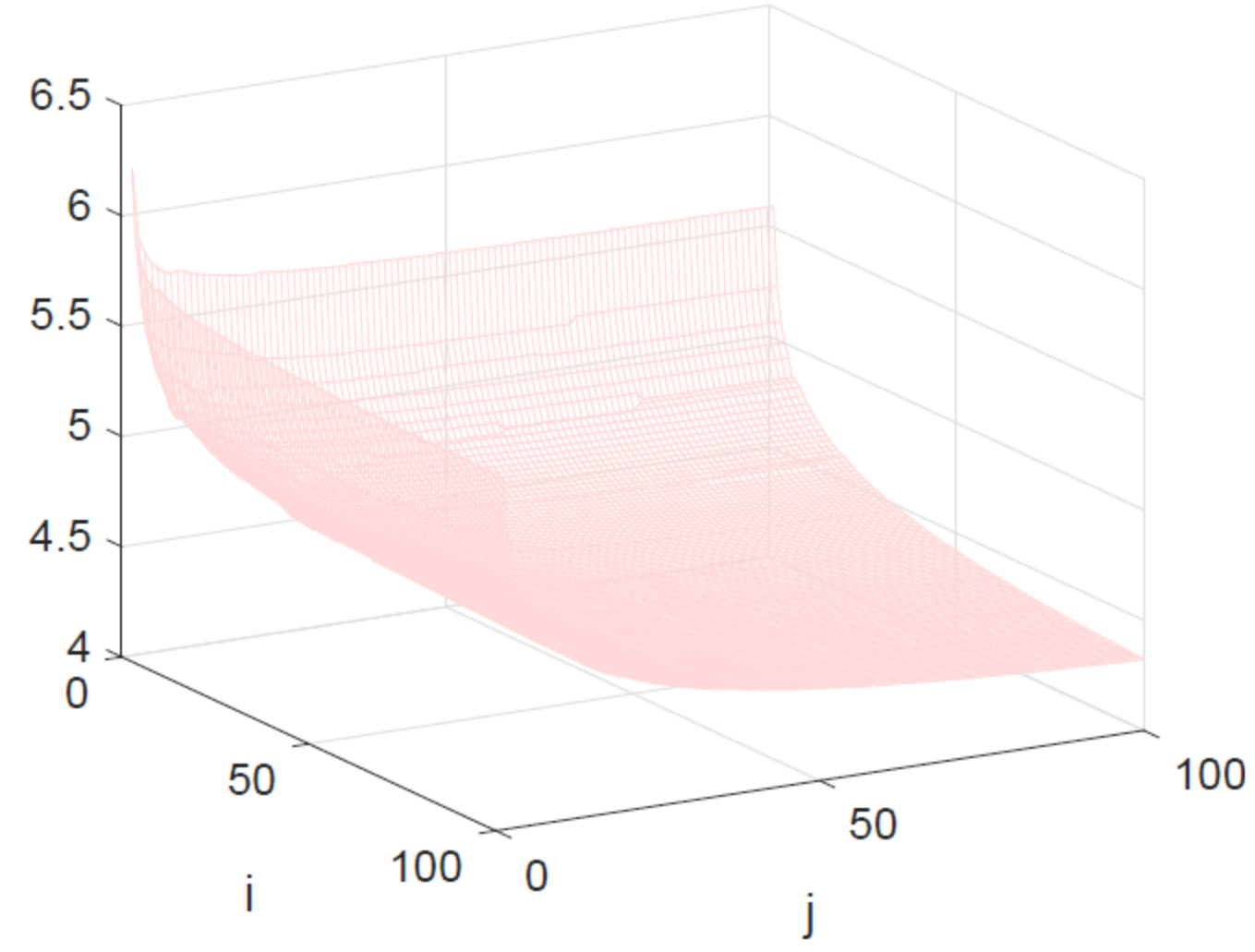
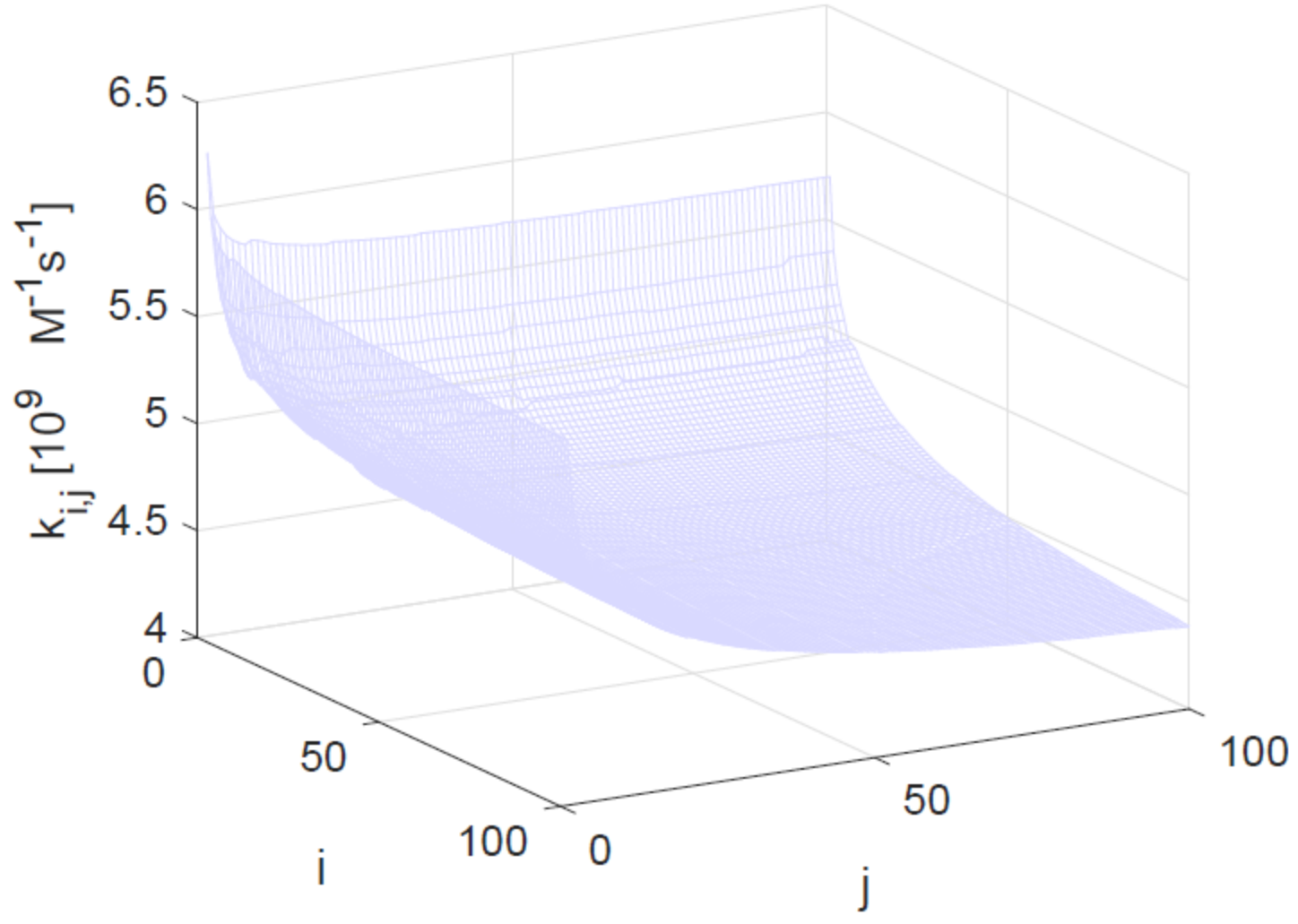
An online supplement to this article can be found by visiting BJ Online at <http://www.biophysj.org>.

**A**

$l_p = 333$

$l_p = 500$

$l_p = 1000$



**B**

$k_{1,j}$

$k_{5,j}$

$k_{20,j}$

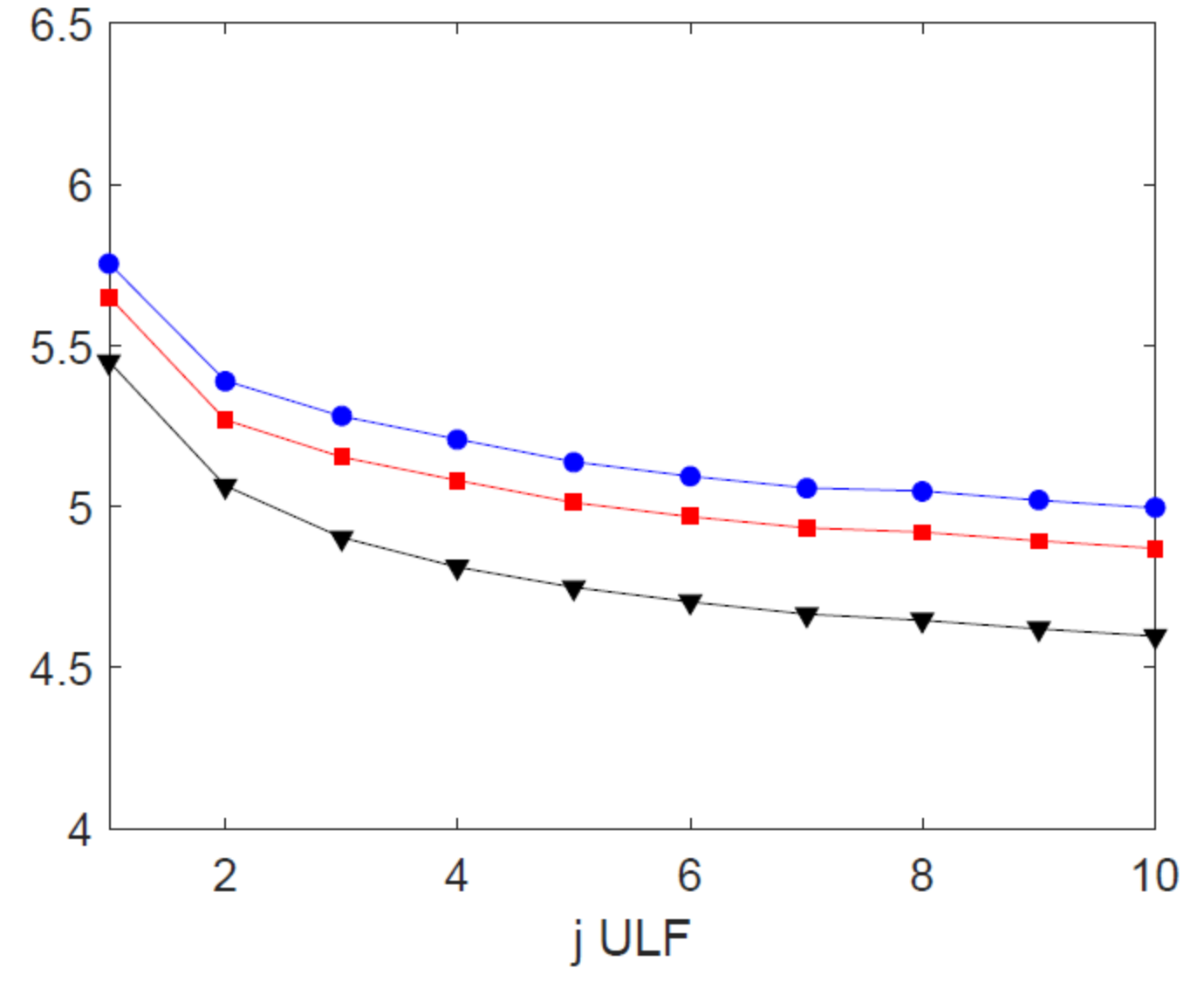
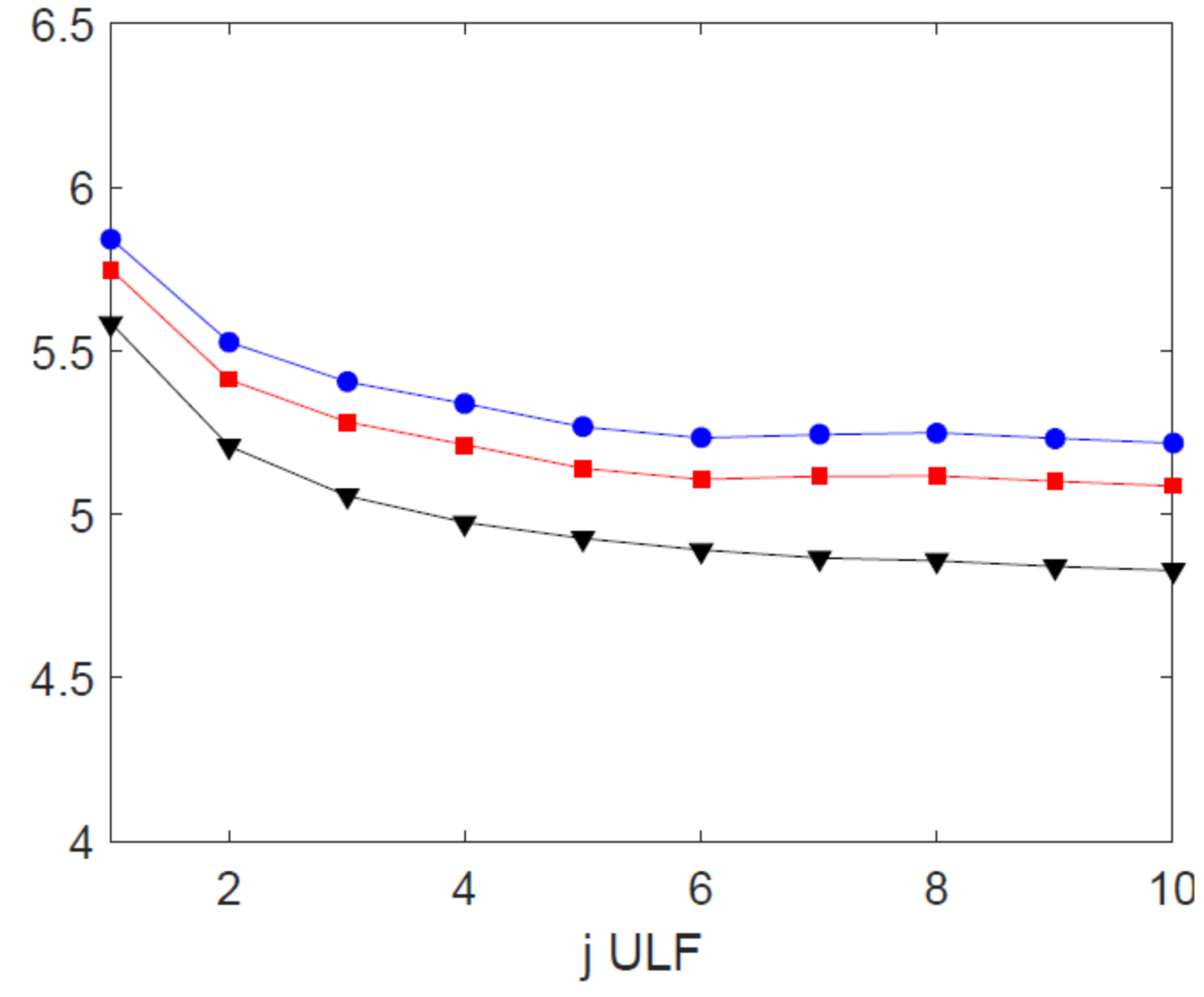
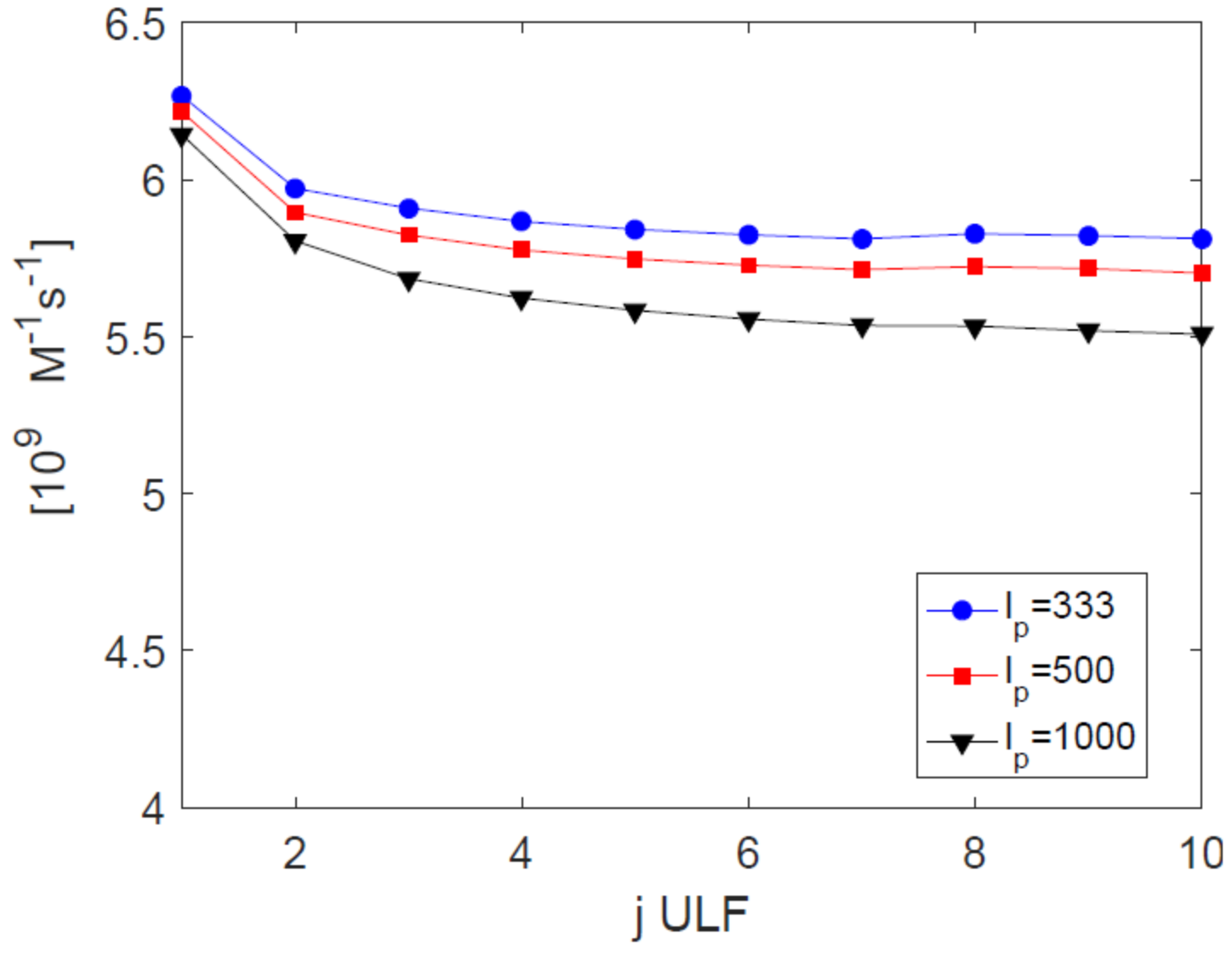
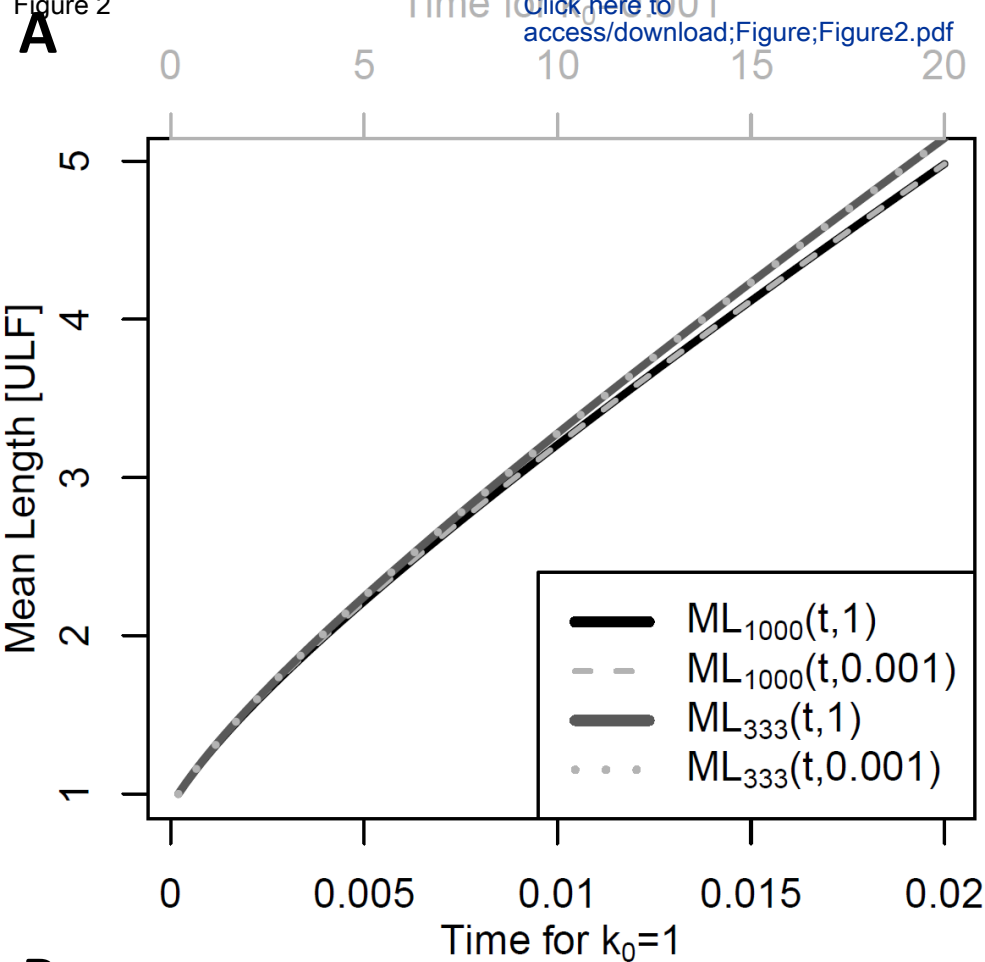


Figure 2

**B**

$l_p = 1000$	$k_0$	1	0.1	0.01	0.001
	$t$	0.021	0.201	2.008	20.08

$l_p = 333$	$k_0$	1	0.1	0.01	0.001
	$t$	0.020	0.192	1.916	19.16

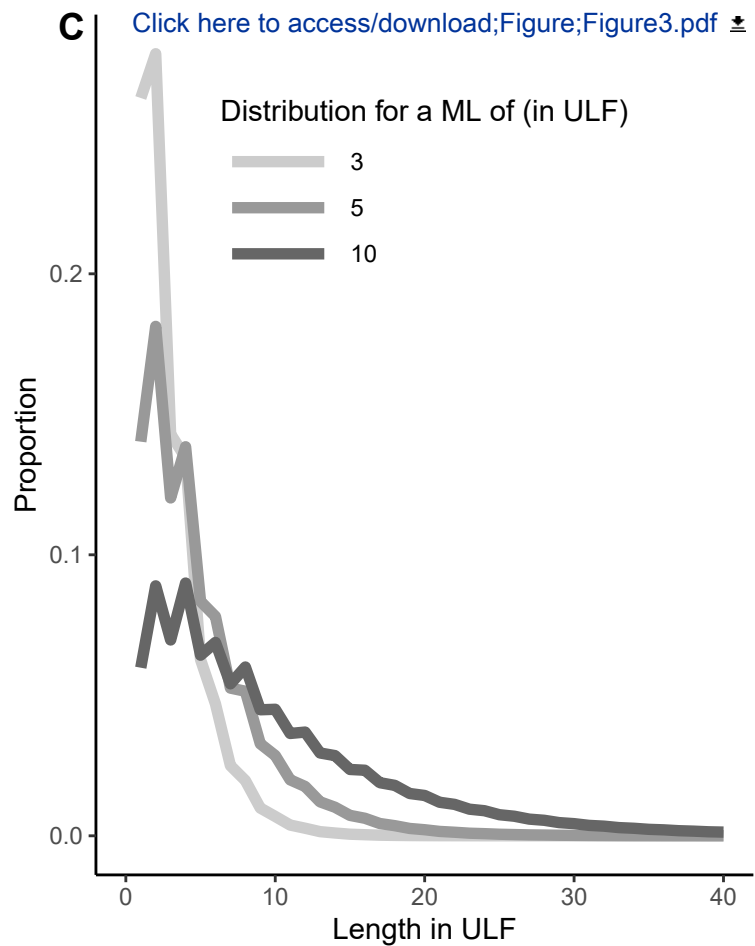
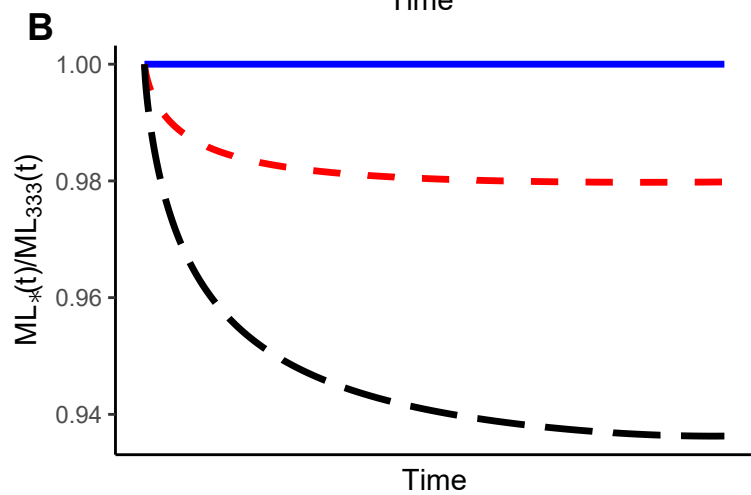
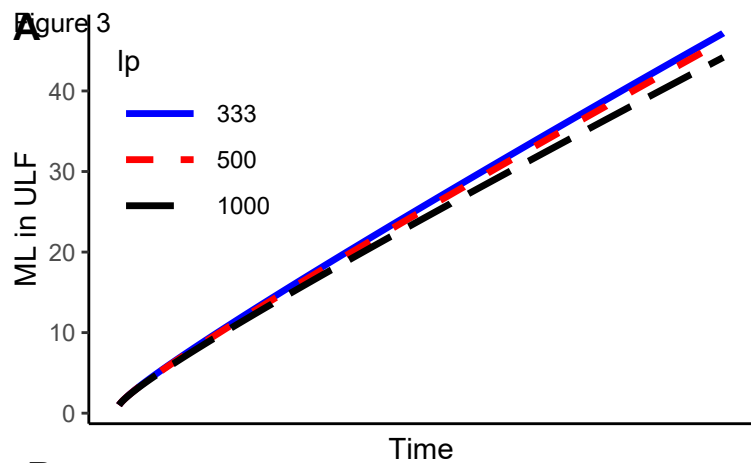
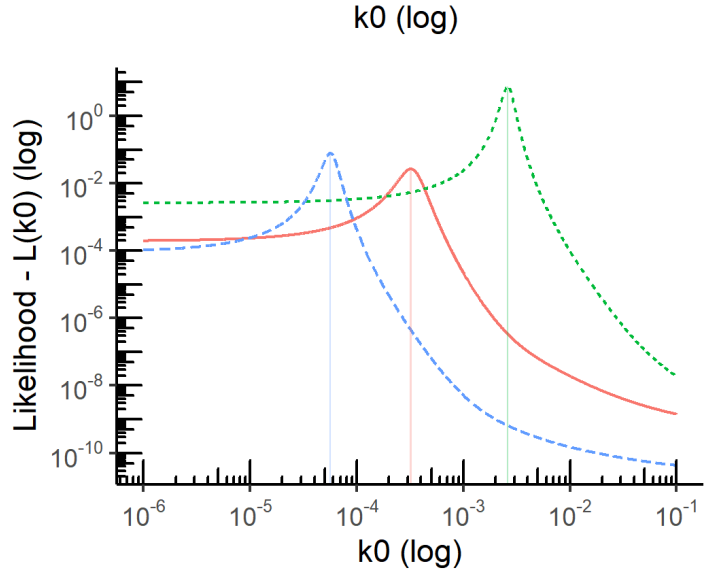
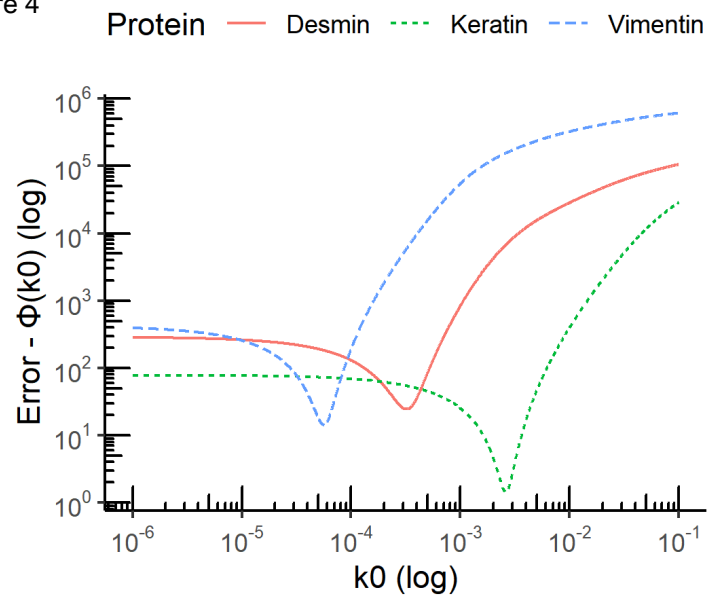


Figure 4



**C**

	Keratin	Desmin	Vimentin
90% IC	$[2.5 \times 10^{-3}, 2.7 \times 10^{-3}]$	$[3.1 \times 10^{-4}, 3.3 \times 10^{-4}]$	$[5.5 \times 10^{-5}, 5.7 \times 10^{-5}]$
$\hat{k}_0$	$2.6 \times 10^{-3}$	$3.21 \times 10^{-4}$	$5.64 \times 10^{-5}$

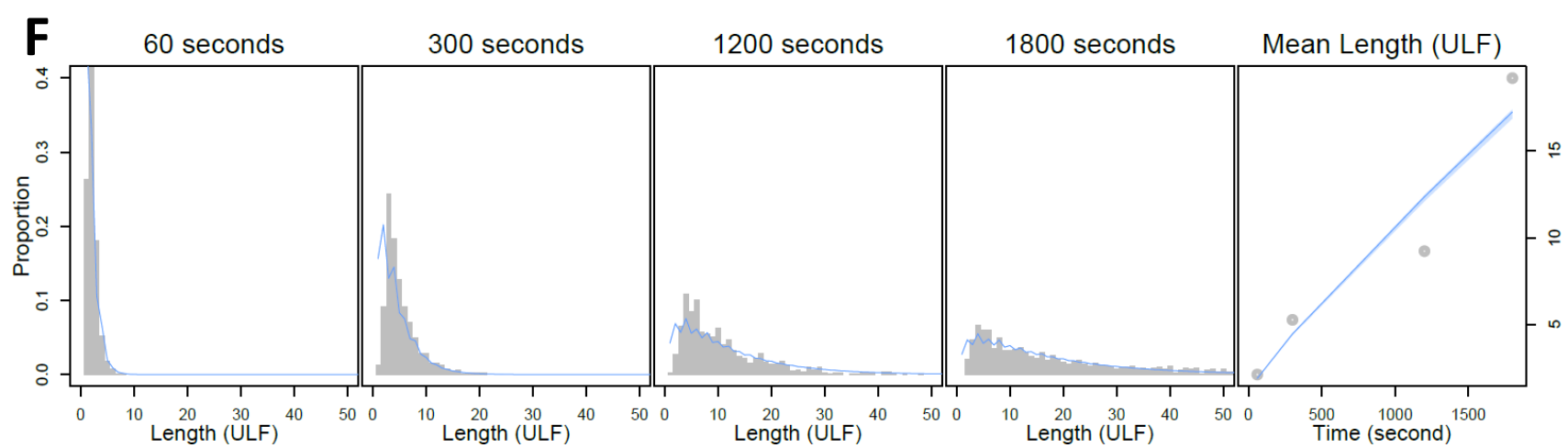
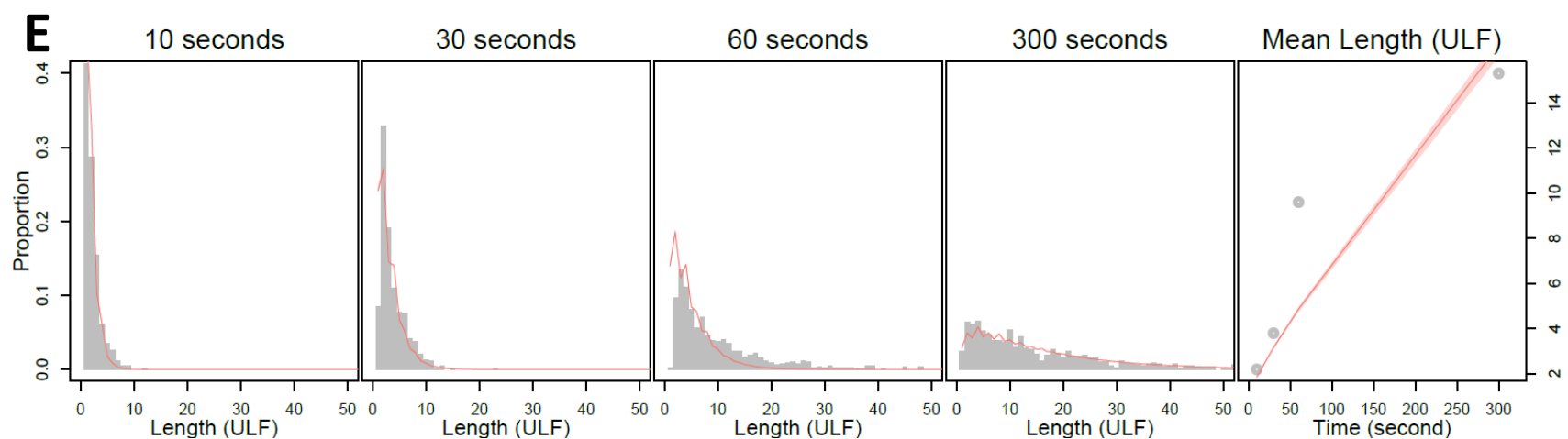
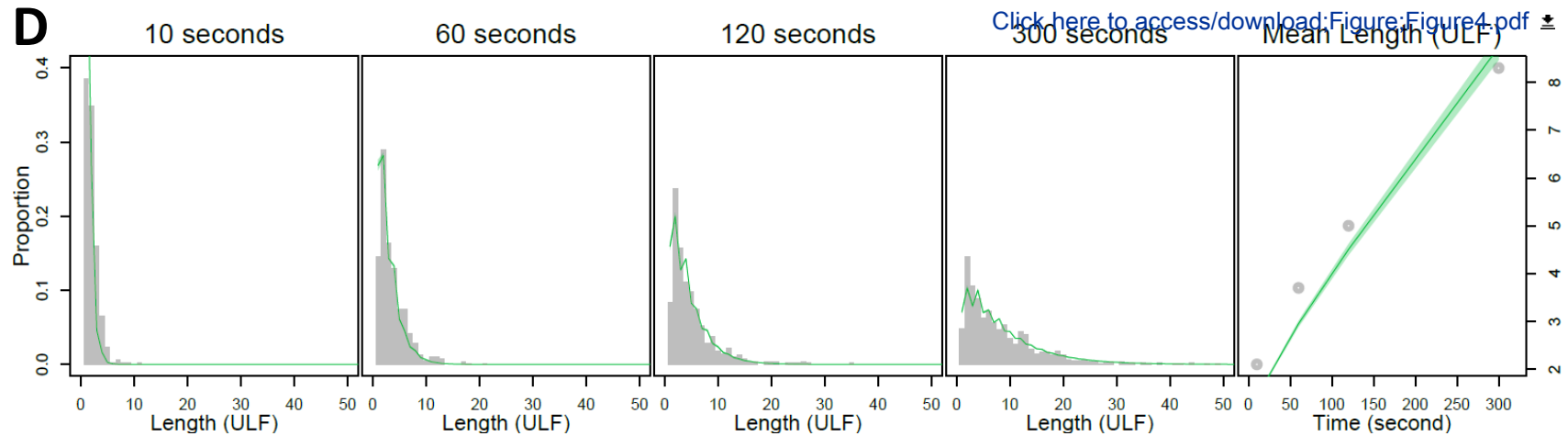
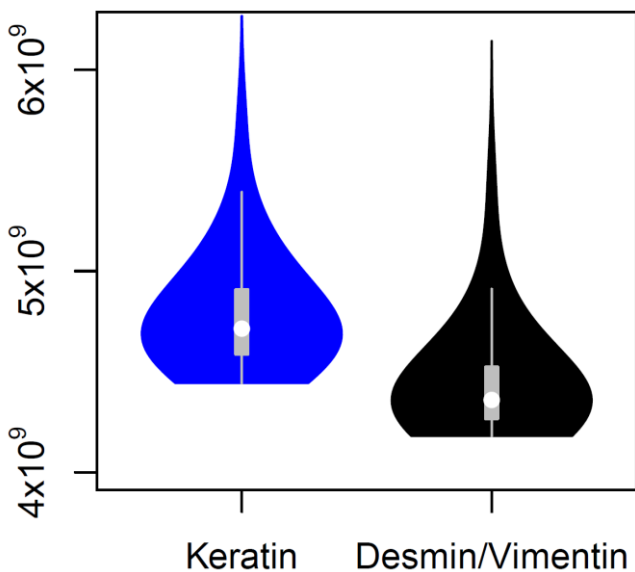

[Click here to access/download:Figure:Figure4.pdf](#)

Figure 5

**A**

Click here to access/download;Figure;  
 $k_{ij}$  ( $M \cdot s^{-1}$ )



**B**

Effective rates ( $M^{-1} \cdot s^{-1}$ )

